This article has been accepted for publication in Monthly Notices of the Royal Astronomical Society *©: 2021 The Authors. Published by Oxford University Press on behalf of the Royal Astronomical Society. All rights reserved.*

Monthly Notices of the ROYAL ASTRONOMICAL SOCIETY

MNRAS **509,** 1160–1174 (2022) https://doi.org/10.1093/mnras/stab3096
Advance Access publication 2021 October 25

Radio relics radio emission from multishock scenario

Giannandrea Inchingolo [1,2]★ D. Wittor,[1,3] K. Rajpurohit [1,2,4] and F. Vazza [1,2,3]

[1]*Dipartimento di Fisica e Astronomia, Università di Bologna, Via Gobetti 92/3, I-40129, Bologna, Italy*
[2]*Institute of Radioastronomy – INAF, Via Gobetti 101, I-40129 Bologna, Italy*
[3]*Hamburger Sternwarte, Gojenbergsweg 112, D-21029 Hamburg, Germany*
[4]*Thüringer Landessternwarte, Sternwarte 5, D-07778 Tautenburg, Germany*

Accepted 2021 October 21. Received 2021 October 18; in original form 2021 July 1

ABSTRACT

Radio relics are giant (∼Mpc) synchrotron sources that are believed to be produced by the (re)acceleration of cosmic ray electrons (CRe) by shocks in the intracluster medium. In this numerical study, we focus on the possibility that some radio relics may arise when electrons undergo diffusive shock acceleration at multishocks in the outskirts of merging galaxy clusters. This multishock (MS) scenario appears viable to produce CRe that emit visible synchrotron emission. We show that electrons that have been shocked multiple times develop an energy spectrum that significantly differs from the power-law spectrum expected in the case of a single shock scenario. As a consequence, the radio emission generated by CRe that shocked multiple times is higher than the emission produced by CRe that are shocked only once. In the case explored in this paper, the radio emission produced in the two scenarios differ by one order of magnitude. In particular in the MS scenario, the simulated relic follows a KGJP spectral shape, consistent with observation. Furthermore, the produced radio emission is large enough to be detectable with current radio telescopes (e.g. LOFAR, JVLA).

Key words: galaxies: clusters: general.

1 INTRODUCTION

Radio relics usually located in the outskirts of merging galaxy clusters are giant (∼Mpc) synchrotron sources that are believed to be produced by cosmic ray electrons (CRe) (re)-accelerated by merger induced shock waves in the intracluster medium (ICM; Ensslin et al. 1998; Roettiger, Stone & Burns 1999; Brunetti & Jones 2014; Bykov et al. 2019; van Weeren et al. 2019). The connection between shocks and relics has been confirmed by finding the surface brightness and temperature discontinuities in the X-ray observations at the location of relics (e.g. Giacintucci et al. 2008; Akamatsu & Kawahara 2013; van Weeren et al. 2019).

The details of the acceleration mechanisms in radio relics are still not fully understood. The widely accepted mechanism for acceleration of relativistic cosmic ray (CR) particles at shock fronts is diffusive shock acceleration (DSA, e.g. Blandford & Eichler 1987). DSA is based on the original idea of Fermi (1949), according to which particles are scattered upstream and downstream of the shock by plasma irregularities, gaining energy at each shock crossing. In recent years, deep X-ray observations performed with *Chandra*, *XMM–Newton*, and *Suzaku* have led to an increase in the number of shocks detected in merging galaxy clusters (e.g. Akamatsu et al. 2017; Canning et al. 2017; Botteon, Gastaldello & Brunetti 2018, for recent works). Radio and X-ray observations suggest that radio relics probe particle acceleration by weak shocks, $\mathcal{M} \leq 5$ (e.g. Bonafede et al. 2009, 2012; van Weeren et al. 2010; Akamatsu et al. 2017; Hoang et al. 2017; Botteon et al. 2018; Rajpurohit et al. 2018; Di Gennaro et al. 2019) in a high-β ($\beta = P_{\rm th}/P_B$, i.e. the ratio between the thermal and magnetic pressures) environment such as the ICM, where the thermal pressure dominates over the magnetic pressure. However, X-ray and radio estimates of shocks' strength are typically in disagreement, possibly because these two proxies probe different parts of the underlying Mach number distribution (see e.g. Wittor et al. 2021, for a recent discussion of this issue). In the weak shock regime, the acceleration efficiencies of cosmic ray protons (CRp) are poorly understood, although current models and simulations predict acceleration efficiencies (defined as the ratio between the shock kinetic power and the energy flux of accelerated CRs) that are less than a few per cent (e.g. Ha et al. 2018; Ryu, Kang & Ha 2019; Ha, Ryu & Kang 2020; Wittor et al. 2020), in agreement with direct constraints coming from γ-ray non-detections of galaxy clusters (e.g. Ackermann et al. 2010, 2014, 2016; Wittor 2021, for review). On the other hand, the observed connection between radio relics and shocks in merging galaxy clusters demonstrates that the electron acceleration (or re-acceleration) at these shocks is efficient, in the sense that even weak shocks ($\mathcal{M} \leq 2$) are associated with detectable radio emission. This implies a surprisingly large ratio of electron-to-proton CR acceleration efficiencies for DSA, because at the same time CR protons have never been detected in the ICM (e.g. Brunetti & Jones 2014; Vazza & Brüggen 2014; Vazza et al. 2015, 2016; Botteon et al. 2020).

Even if radio power of some relics can be explained by the acceleration of electrons from the thermal pool (i.e. DSA mechanism) (Locatelli et al. 2020), this mechanism alone cannot explain the high radio power of the majority of relics (Botteon et al. 2016; Eckert et al. 2016; Hoang et al. 2017). To mitigate the problem of the high acceleration efficiencies implied by weak cluster shocks, recent

★ E-mail: giannandr.inchingolo@unibo.it

© 2021 The Author(s)
Published by Oxford University Press on behalf of Royal Astronomical Society

theoretical models assume a pre-existing population of CRe at the position of the relic that is re-accelerated by the passage of the shock (e.g. Markevitch et al. 2005; Kang & Ryu 2011; Macario et al. 2011; Kang, Ryu & Jones 2012; Pinzke, Oh & Pfrommer 2013; Kang et al. 2014; Botteon et al. 2020). This would soften the above theoretical problems, because the population of CRs processed by $\mathcal{M} \leq 3$–4 shocks is predicted to be dominated by the re-accelerated fossil populations, and not the freshly accelerated one. The re-acceleration scenario is supported by the observation of radio galaxies located nearby or within a few radio relics (e.g. Bonafede et al. 2014; Shimwell et al. 2015; Botteon et al. 2016; van Weeren et al. 2017; Di Gennaro et al. 2018). However, it is not obvious that the injection of fossil electrons by one or a few radio galaxies, can automatically produce a uniform population of electrons, capable of producing the high degree of coherence of the radio emission observed in a few giant relics: in radio relics like 'the Sausage' and 'the Toothbrush' the spectral properties of the emission are very coherent across ∼2 Mpc, requiring a very uniform distribution of coeval fossil electrons in the shock upstream (e.g. van Weeren et al. 2010, 2016; Di Gennaro et al. 2018; Rajpurohit et al. 2018, 2020).

Complementary to the above scenario, we thus focus here on a specific mechanism potentially alleviating this problem, i.e. we consider a multishock (MS) scenario in which multiple, wide merger shocks sweeping the ICM in sequence can produce a large-scale and uniform distribution of mildly relativistic electrons. A similar mechanism has been very recently analysed by Kang (2021), in the context of the acceleration of CRp via DSA. The existence of multiple populations of shock waves sweeping the ICM along a variety of angles with respect to the leading axis of mergers, and possibly merging into larger shocks have been recently explored by several simulations (e.g. Hong, Kang & Ryu 2015; Zhang et al. 2020; Zhang, Churazov & Zhuravleva 2021).

In our work, we focus on MS electron acceleration and the radio emission generated in this way. In detail, we analyse the simulation of a massive $M_{200} \approx 9.7 \times 10^{14}\,\mathrm{M}_{\odot}$ galaxy cluster from $z = 1$ to $z = 0$ (Wittor, Vazza & Brüggen 2017), and we compute the radio emission generated by particles following the merging of the cluster, showing that MS electrons develop, on average, large enough radio emission to be detectable with current radio telescopes (e.g. LOFAR).

This paper is organized as follows: In Section 2, we describe the numerical set-up used for the galaxy cluster simulation and the model used to simulate the evolution of electron spectra. The results obtained are analysed in Section 3, where we distinguish two different relics probed by the particle simulated and we study the radio emission of these particles catalogued by their shock history. The detailed study of the integrated radio emission is presented in Section 4. Section 5 summarizes the results obtained in the paper and discusses future work.

2 NUMERICAL METHOD

2.1 Simulation set-up

In this work, we study a massive, $M_{200} \approx 9.7 \times 10^{14}\,\mathrm{M}_{\odot}$, galaxy cluster that was simulated and analysed in Wittor, Vazza & Brüggen (2016) and Wittor et al. (2017). This cluster is interesting for a comparison with real observations as it undergoes a major merger at redshift $z \approx 0.27$, producing detectable giant radio relics. The cluster was simulated with the cosmological magnetohydrodynamic (MHD) code ENZO (Bryan et al. 2014) and analysed with the Lagrangian tracer code Cosmic-Ray Tracers (CRATER) (Wittor et al. 2017). In the following, we give a brief overview on the used simulation set-up. For specific details, we point to section 2.1 in Wittor et al. (2017).

The ENZO code follows the dark matter using a *N*-body particle-mesh solver (Hockney & Eastwood 1988) and the baryonic matter using an adaptive mesh refinement (AMR) method (Berger & Colella 1989). More specifically, Wittor et al. (2017) used the piecewise linear method (Colella & Glaz 1985) in combination with the hyperbolic Dedner cleaning (Dedner et al. 2002). The simulation covers a root grid with a comoving volume of $\sim(250\,\mathrm{Mpc})^3$ sampled with 256^3 grid cells and dark matter particles. An additional comoving volume of size $\sim(25\,\mathrm{Mpc})^3$ has been further refined using five levels of AMR, i.e. 2^5 refinements, for a final resolution of 31.7 kpc. The chosen AMR criteria, i.e. based on the overdensity and the 1D velocity jump, ensure that about ~ 80 per cent of the cluster volume are refined at the highest AMR level.

We study this cluster in detail because it is a massive one, it has been already the subject of several works by our group, and because the fairly large dynamical range and number of available snapshots is optimal for our analysis involving tracer particles (see below). However, the final magnetic field reached through small-scale dynamo amplification in this object is kept artificially small by the spatial resolution, which is not enough to ensure a large enough Reynolds number to enter an efficient small-scale dynamo amplification regime, as studied in Vazza et al. (2018). Therefore, for simulating the injection and advection of CRe in this system, we re-normalized the magnetic field strength, measured by the tracers, by a factor 10. The re-normalization results typical magnetic field strengths of ∼0.1–0.2 μG in our relics. In fact, the electron cooling depends rather weakly on the renormalization of magnetic field strengths, because inverse Compton cooling dominates over synchrotron cooling (see the denominator in equation 5).

Using CRATER, Wittor et al. (2017) used a total of $\sim 1.3 \times 10^7$ Lagrangian tracer particles to analyse the cluster's evolution between $z = 1$ and $z = 0$, at a (nearly constant) time resolution of $\Delta t = 31$ Myr. Following the gas distribution of the ICM, CRATER injects particles with a fixed mass, i.e. in our case $m_{\mathrm{tracer}} \approx 10^8\,\mathrm{M}_{\odot}$, into the simulation. The tracers' velocities are computed by interpolating the local velocities to the tracers' position using a *cloud-in-cell*-interpolation method. An additional velocity correction term was used in Wittor et al. (2017) to account for mixing motions that might be underestimated in the case of complex flows (Genel et al. 2013). The velocity interpolation schemes have been extensively tested in Wittor et al. (2017) and Wittor (2017).

The tracer particles use a temperature-based shock finder to detect shocks in the ICM. The corresponding Mach number is computed from the Rankine–Hugoniot relation, assuming $\gamma = 5/3$, as

$$M = \sqrt{\frac{4}{5}\frac{T_{\mathrm{new}}}{T_{\mathrm{old}}}\frac{\rho_{\mathrm{new}}}{\rho_{\mathrm{old}}} + \frac{1}{5}}. \quad (1)$$

Here, T and ρ are the temperature and density in the pre- and post-shock.

We have specifically chosen the cluster simulation presented in Wittor et al. (2016, 2017) for our analysis. Wittor et al. (2017) found that a significant fraction of the particles that produce giant radio relics at $z \approx 0$, have crossed several shocks before, see fig. 12 and section 3.5 therein. Hence, the radio emitting particles should have been subjected to several cycles of shock (re-)acceleration, making this simulation a perfect candidate for our analysis.

We use a 3D rendering of this merger event to better describe the sequence of mergers (leading to MS waves) which interest a particular sector of the cluster. Fig. 1 shows a snapshot sequence

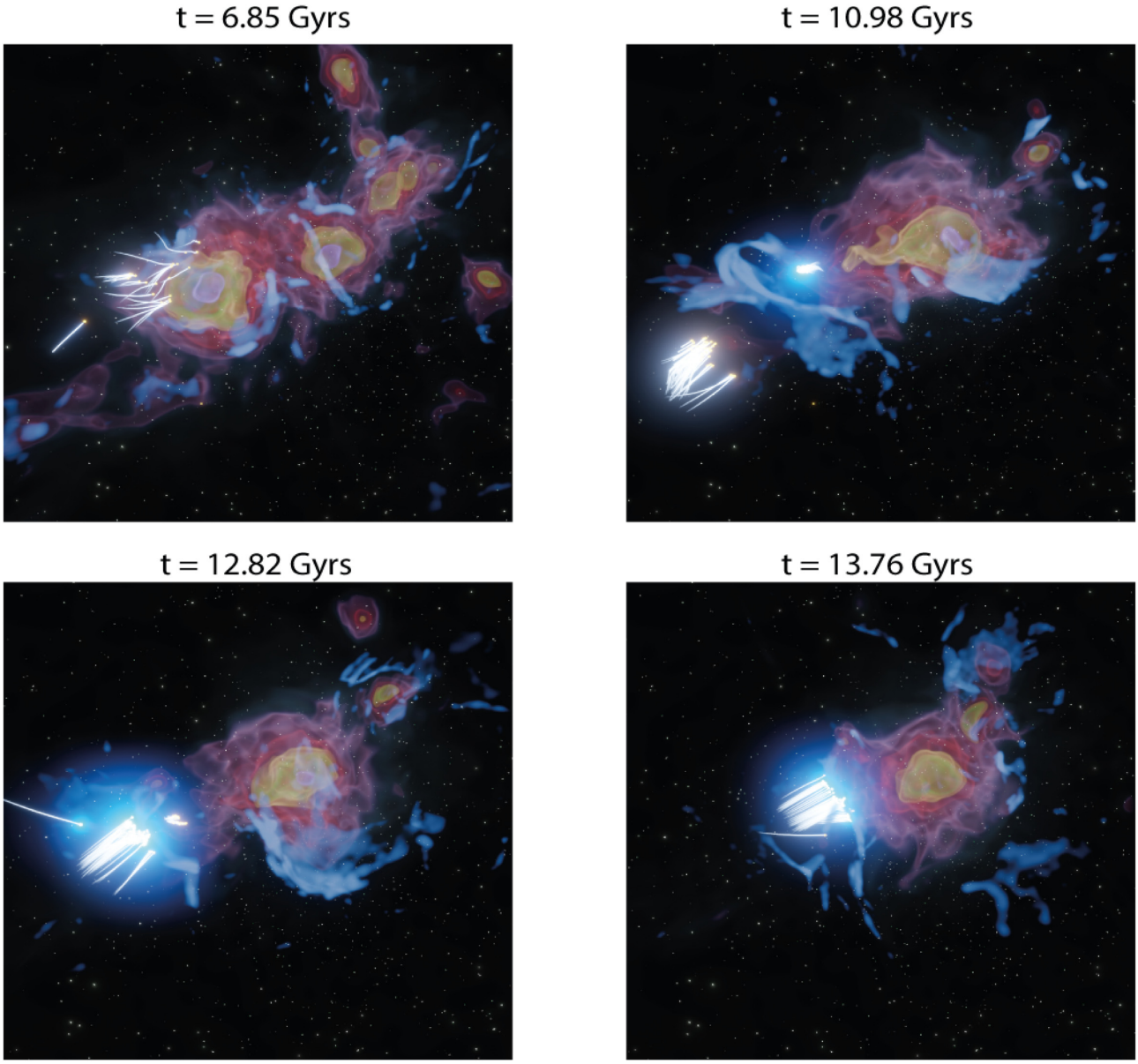

Figure 1. Snapshot sequence at different times of, respectively, the galaxy cluster baryonic density (purple–yellow), the radio emission at 1.4 GHz (light blue), and the tracers with their path. The tracers change from yellow (not active) to blue (active) when they cross a shock front in the simulation.

obtained from a cinematic scientific visualization realized from the simulation data.[1] The video shows the baryonic density (purple–yellow) surrounded by the volumetric radio emission at 1.4 GHz (light blue) during the formation of the galaxy cluster. The tailed spheres highlight the evolution of a selection of tracers. Initially, all the tracers are yellow and when they cross a shock front, they are activated, changing colour to bright blue. The sequence in Fig. 1 shows the evolution of two streams of tracers ('beam'). This qualitative analysis of the cluster merging evolution shows a history of MS scenario before tracers arrive at the end of the simulation. In this paper, we analyse the spectral evolution measured by the tracers in this simulation.

2.2 Simulating the evolution of electron spectra

We solve the time-dependent diffusion-loss equation of relativistic electrons represented by tracer particles, using the standard Chang & Cooper (1970) finite-difference scheme implemented in a serial code written in IDL language. We used $N_b = 10^5$ equal energy bins in the $\gamma_{min} \leq \gamma \leq \gamma_{max}$ Lorentz factor, with $\gamma_{min} = 1$ and $\gamma_{max} = 4.5 \times 10^5$ (hence $d\gamma = 5$). The code we used to evolve our particle spectra is freely available.[2]

We are concerned with the evolution of relativistic electrons injected and/or re-accelerated by shocks, at the periphery of clusters

[1]The video is called '*The VLA shedding lights on the origin of radio relics*' and it was recently awarded the first prize for the NRAO Image Contest for the celebration of VLA 40th anniversary. The video is available at the following link: https://vimeo.com/464248944/3fc17a5b8b.

[2]https://github.com/FrancoVazza/IDL_FP

and on time-scales of a few Gigayears (≤ 3 Gyr). For this specific task, we only have to evolve the energy spectra for ∼7000 tracers, necessary to sample the spatial extension of radio relics formed in the system by $z \approx 0$. The combination of the limited amount of tracers and of the relatively small number of snapshots to process (up to 238) allowed us to resort to the serial implementation of the Fokker Planck solver already used in previous work (e.g. Rajpurohit et al. 2020). Notice that, unlike the more recent work presented in Vazza et al. (2021), in this implementation, we evolve the electron spectra in γ space, and not in momentum space. This introduces a small error in the low-energy part of the spectra, where the injected distribution from shock acceleration is a power law in momentum space, but not in γ space (since of course $E^2 = m^2c^4 + p^2c^2$). The ultra-relativistic simplification used here is however suitable when focusing on the radio emitting electrons ($\gamma \geq 10^2 - 10^3$) and also considering that the accumulated particle population at low energy is small in the short time range considered (e.g. Sarazin 1999).

We considered a reduced Fokker–Planck equation without injection and escape terms (i.e. Liouville equation), and neglected the spatial diffusion of CRs (which is appropriate for the ∼MeV–GeV electrons considered in this work), which allows us to track the evolution of the number density of relativistic electrons as a function of their energy, $N(\gamma)$, computed separately for each tracer particle:

$$\frac{\partial N}{\partial t} = \frac{\partial}{\partial \gamma}\left[N\left(\left|\frac{\gamma}{\tau_{\rm rad}}\right| + \left|\frac{\gamma}{\tau_{\rm c}}\right| + \frac{\gamma}{\tau_{\rm adv}} - \left|\frac{\gamma}{\tau_{\rm acc}}\right|\right)\right]. \quad (2)$$

We use the approximation

$$\dot{\gamma} \approx \left|\frac{\gamma}{\tau_{\rm rad}}\right| + \left|\frac{\gamma}{\tau_{\rm c}}\right| + \frac{\gamma}{\tau_{\rm adv}} - \left|\frac{\gamma}{\tau_{\rm DSA}}\right|, \quad (3)$$

where $\tau_{\rm rad}$, $\tau_{\rm c}$, and $\tau_{\rm adv}$ are, respectively, the loss time-scales for the radiative, Coulomb and expansion (compression) processes that we define in Section 2.2.1. $\tau_{\rm DSA}$ represents instead the acceleration time-scale due to DSA that we estimate in Section 2.2.2.

The numerical solution is obtained using the Chang & Cooper (1970) finite difference scheme:

$$N(\gamma, t + {\rm d}t) = \frac{N(\gamma, t)/{\rm d}t + N(\gamma + {\rm d}\gamma, t + {\rm d}t)\gamma}{1/{\rm d}t + \gamma/{\rm d}\gamma} + Q_{\rm inj}(\gamma), \quad (4)$$

where in the adopted splitting-scheme to perform the finite differences we assumed $N(\gamma + {\rm d}\gamma/2) = N(\gamma + {\rm d}\gamma)$ and $N(\gamma - {\rm d}\gamma/2) = N(\gamma)$, where $Q_{\rm inj}$ accounts for the injection by shocks. The latter is regarded as an almost instantaneous process, considering that time-scales are much shorter than the time-step of our integration, $\delta t \approx 31$Myr (see equation 10 below).

2.2.1 *Loss terms*

The time-scales associated with the energy losses by radiative, Coulomb, and expansion (compression) processes are given by the following formulae, adapted from Brunetti & Jones (2014):

$$\tau_{\rm rad} = \frac{7720\ {\rm Myr}}{(\gamma/300)\left[\left(\frac{B}{3.25\,\mu{\rm G}}\right)^2 + (1+z)^4\right]}, \quad (5)$$

$$\tau_{\rm c} = 7934\ {\rm Myr}\left\{\frac{n/10^{-3}}{\gamma/300}\left(1.168 + \frac{1}{75}\ln\left(\frac{\gamma/300}{n/10^{-3}}\right)\right)\right\}^{-1}, \quad (6)$$

and

$$\tau_{\rm adv} = \frac{951\ {\rm Myr}}{\nabla\cdot\mathbf{v}/10^{-16}}, \quad (7)$$

where the density n is measured in cm^{-3}, B in μG, and the gas divergence $\nabla\cdot\mathbf{v}$ is measured in s^{-1}. Bremsstrahlung losses can be safely neglected in this case, because for the typical ICM conditions encountered also their time-scale is much larger than the ones of all other loss channels. Inverse Compton and synchrotron losses are by far the most relevant for the evolution of electrons considered in this work, owing to their peripheral location and low gas density.

2.2.2 *Shock (re-)acceleration*

Predicting the spectrum of injected 'fresh' relativistic electrons injected by weak shocks, as well as their spectrum after shock re-acceleration, is far from being a solved problem. In this paper, we follow a relatively simple approach, motivated by the existing literature on the subject and meant to simplify the steps to determine the post-shock spectrum of radio emitting electrons.

We rely here on the DSA model by Kang & Ryu (2011), which assumes that the injection Lorentz factor of electrons is related to the injection momentum ($\gamma_{\rm inj} = \sqrt{1 + p_{\rm inj}^2/m_{\rm e}^2c^2}$), where $p_{\rm inj}$ in DSA is assumed to be a multiple of the thermal momentum of *protons*, i.e. $p_{\rm inj} = \xi p_{\rm th}$ ($p_{\rm th} = \sqrt{2k_{\rm b}T_{\rm d}m_p}$, where $k_{\rm b}$ is the Boltzmann constant). Following Kang & Ryu (2011), we compute ξ based on the fit formula given from their one-dimensional convection–diffusion simulations:

$$\xi_{\rm inj} = 1.17\frac{m_p v_{\rm d}}{p_{\rm th}}\left(1 + \frac{1.07}{\epsilon_B}\right)\frac{\mathcal{M}^{0.1}}{3^{0.1}}, \quad (8)$$

where $v_{\rm d}$ is the downstream shock velocity and ϵ_B is the ratio of magnetic field strength between the B_0 downstream magnetic field generated by the shock, and $B_\perp$ is the magnetic field perpendicular to the shock normal. We set here $\epsilon_B = 0.23$ (Pinzke et al. 2013) and obtaining values in the range $\xi_{\rm inj} \sim 2.5-3.5$ and $\gamma_{\rm inj} \sim 10-20$ for our shocks.

The source term for relativistic electrons in equation (4) assumes an energy distribution that follows a power law (e.g. Kardashev 1962; Sarazin 1999):

$$Q_{\rm inj}(\gamma) = K_{\rm inj,e}\,\gamma^{-\delta_{\rm inj}}\left(1 - \frac{\gamma}{\gamma_{\rm cut}}\right)^{\delta_{\rm inj}-2}, \quad (9)$$

in which the initial slope of the input momentum spectrum, $\delta_{\rm inj}$, is computed based on the standard DSA prediction, i.e. $\delta_{\rm inj} = 2(\mathcal{M}^2 + 1)/(\mathcal{M}^2 - 1)$. The cuff-off energy, $\gamma_{\rm cut}$, is defined for every shocked tracer as the maximum energy, beyond which the radiative cooling time-scale is shorter than the acceleration time-scale, $\tau_{\rm DSA}$:

$$\tau_{\rm DSA} = \frac{3}{V_{\rm s}^2}\frac{D(E)}{r-1}\frac{r(r+1)}{r-1}, \quad (10)$$

where r is the shock compression factor, $V_{\rm s}$ is the shock velocity, and $D(E)$ is the diffusion coefficient of relativistic electrons, as a function of their energy (e.g. Gabici & Blasi 2003). The specific energy-dependent value of $D(E)$ is little constrained because it depends on the local conditions of the turbulent plasma, and it is critical to limit the maximum energy in DSA (e.g. Kang et al. 2012). However, the latter is not an issue for our simulation, because all plausible choices of $D(E)$ in equation (10) give an acceleration time-scale many orders of magnitude smaller than the typical cooling time of radio emitting electrons, whose energy distribution be assumed to follow a power law within the energy range of interest, at least the moment of their injection. We can set therefore $\gamma_{\rm cut} = \gamma_{\rm max}$ in this work.

This also motivates the fact that we can model shock injection by DSA by adding the newly created population of particles across time-

Table 1. Tracer population statistic in the different families for both Relic A and Relic B.

	Relic A		Relic B	
Family 1	1297	91.92 per cent	1709	28.91 per cent
Family 2	114	8.08 per cent	3687	62.36 per cent
Family 3			489	8.27 per cent
Family 4			27	0.46 per cent
Total	1411		5912	

steps (see equation 4), without integrating a source term as needed for the much slower re-acceleration by turbulence (see below).

Under these assumptions, the rate of injection of relativistic electrons in the downstream is

$$K_{\rm inj,e} = 4\pi\ K_{\rm e/p} \int_{p_{\rm inj}}^{p_{\rm cut}} \left(\sqrt{p^2+1}-1\right) f_{\rm N}\ p^{-(\delta_{\rm inj}+2)} \times \exp\left[-(p/p_{\rm cut})^2\right]\ p^2 {\rm d}p\ {\rm d}x_{\rm t}^2\ V_{\rm s}\ {\rm d}t, \quad (11)$$

with

$$f_{\rm N} = \frac{n_{\rm d}}{\pi^{3/2}} p_{\rm th}^{-3} \exp\left(-\xi_{\rm inj}^2\right), \quad (12)$$

where $K_{\rm e/p}$ is the electron-to-proton ratio. Following Kang (2020), we use $K_{\rm e/p} = (m_{\rm p}/m_{\rm e})^{(1-\delta_{\rm inj})/2}$, which gives $K_{\rm e/p} \sim 10^{-2}$ for an injection spectral index of $\delta_{\rm inj} \approx 2.3$, in line with the injection spectral index of local Galactic supernova remnants (e.g. Uchiyama et al. 2007).

${\rm d}x_{\rm t}^2$ is the surface element associated with each shocked tracer particle, and is computed considering that ${\rm d}x_{\rm t}^3 = {\rm d}x^3/n_{\rm tracers}$ is the initial volume associated with every tracer at the epoch of their injection ($n_{\rm tracer}$ being the number of tracers in every cell) and ${\rm d}x_{\rm t}(z)^3 = {\rm d}x_t^3 \cdot \rho_{\rm t}/\rho(z)$ is the relative change of the volume associated with each tracer as a function of z, based on the ratio between the density at injection, ρ and the density of cells where each tracer sits as a function of redshift, $\rho(z)$.

This procedure allow us to guess the acceleration efficiency of relativistic electrons at the shock, at least to a first degree of approximation and with a modest computing time. Of course, the physical uncertainty behind this is of course very large, and dedicated simulations are needed to fully solve the acceleration cycle of relativistic electrons by weak merger shocks, for the possible range of shock obliquities and typical plasma conditions of the ICM (Guo, Sironi & Narayan 2014; Park, Caprioli & Spitkovsky 2015; Kang, Ryu & Ha 2019; Xu, Spitkovsky & Caprioli 2020; Ha et al. 2021).

Beside the *direct* injection of relativistic electrons by shocks, we also include the effect of shock *re*-acceleration on existing relativistic electrons (e.g. Markevitch et al. 2005; Kang & Ryu 2011; Kang et al. 2012). According to DSA, the input particle spectrum, $N_0(x)$, becomes

$$N(\gamma) = (\delta_{\rm inj}+2)\gamma^{-\delta_{\rm inj}} \int_{\gamma_{\rm min,re}}^{\gamma} N_0(x) x^{\delta_{\rm inj}+1} {\rm d}x, \quad (13)$$

where $\delta_{\rm inj}$ is the local slope within each energy bin. We consider that the minimum momentum for the electron re-acceleration by shocks is the injection momentum $p_{\rm inj}$, above which DSA is expect to operate (Kang 2020). So we set $\gamma_{\rm min,re-e} = \gamma_{\rm inj}$ as a lower bound for the integration in equation (13).

3 MS SCENARIO OF ELECTRONS RE-ACCELERATION

In this section, we analyse the properties of tracer particles used to probe the evolution of the simulation, focusing on their shock time. We select more than 7000 tracers that cross shocks with Mach number

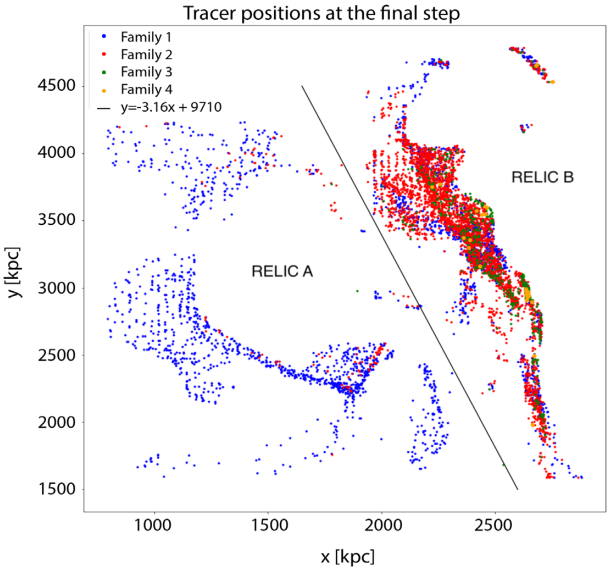

Figure 2. 2D map of the tracer position at the final step. We distinguish two relics for the analysis. The black oblique line (defined by the equation in the legend) divides the region of the two relics, namely Relic A (left) and Relic B (right).

$M \geq 2$ during the entire evolution of the simulation. By construction, all these tracers cross a shock at the end of the simulation $t_{\rm end} = 13.76$ Gyr. We investigate if these tracers crossed other shocks before the final one and if, how many times. We divide the tracers in different families according to the number of shocks they cross during the simulation evolution. Tracers of Family 1 are only accelerated by the shock at the end of the simulation. Families 2, 3, and 4 have been shocked, respectively, one, two, and three times before they cross the final shock. Details of the families population are collected in Table 1.

Fig. 2 shows the (x, y) projection of Family 1 (blue), Family 2 (red), Family 3 (green), and Family 4 (orange) tracers at $t_{\rm end}$. According to these positions, we divide the tracers in two groups named 'Relic A' and 'Relic B' in Fig. 2. We observe that Relic A is composed mostly by Family 1 tracers, with the presence of 8 per cent of Family 2 tracers. Relic B, instead, is composed of more than 62 per cent by Family 2 tracers and for $\sim$ 28 per cent by Family 1 tracers, with the presence of families with higher number of shocks, as reported in Table 1. As first approach, also motivated by the fact that the differences in the timing of shocks within each family of electrons is typically $\leq$ Gyr, we computed the energy evolution of each family based on the family-averaged fields, i.e. assuming at each time-step that the entire family of particles is charactersied by the same values of density, temperature and magnetic field, and that all particles in the same family are shocked at the same time. For this family-averaged analysis, we chose the shock times of each family as the ones at which the majority of the tracers cross a shock simultaneously. This is of course a gross approximation, but it is enough to allow us to obtain some first important information on the electron energy spectrum based on the MS scenario and the subsequent radio emission. A detailed report of the family-averaged approach is available as Appendix of this paper A.

3.1 Relic A

For Relic A, the family-averaged quantities are collected in Table 2. We use these quantities to compute the time evolution of the electron energy spectrum according to the model introduced in Section 2.2.

Table 2. Family-averaged quantities at selected shock times for families in Relic A.

	Time (Gyr)	Mach	B (μG)	ρ (g cm^{-3})	T (K)
Family 1					
Shock 1	13.76	2.6	1.7×10^{-1}	1.3×10^{-28}	2.5×10^{7}
Family 2					
Shock 1	12.69	3.8	1.1×10^{-1}	1.6×10^{-28}	2.7×10^{7}
Shock 2	13.76	2.3	2.2×10^{-1}	2.0×10^{-28}	3.1×10^{7}

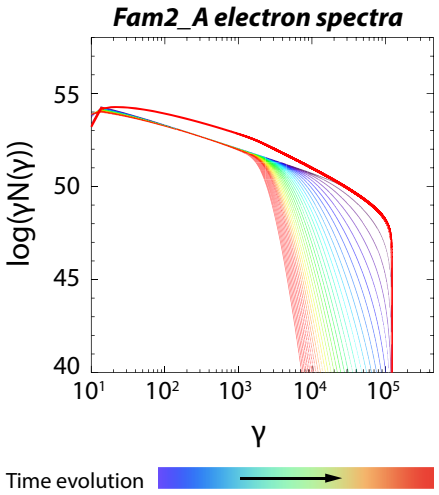

Figure 3. Electron energy spectra time evolution for population-averaged quantities Family 2 tracers in Relic A. Dashed lines correspond to spectra evolution after the first shock. The red solid line represents the electrons spectrum after the second shock.

Fig. 3 shows the time evolution of the electron energy spectrum for Family 2 population for Relic A. The electron population is produced by the first shock at $t_1 = 12.69$ Gyr with a power-law spectrum (purple dashed line of the spectrum) and, as time evolves, we observe a cooling of the high-energy tail of the spectrum, that corresponds to a cut-off at $\gamma \sim 10^3$ right before the second shock. After the final shock at $t_{\rm end} = 13.76$ Gyr, we observe that the electron energy spectrum is no longer a power law and electrons are accelerated up to $\gamma \sim 10^5$ with a soft knee in the slope around $\gamma \sim 10^3$, in correspondence of the cut-off energy before the shock. (red solid line of the spectrum). However, we are cautious about the result in the low-energy part of the spectra, considering the limit of the Fokker–Planck code described in Section 2.2.

3.2 Relic B

For Relic B, the family-averaged quantities are reported in Table 3. We use these quantities to compute the time evolution of the electron energy spectrum according to the model introduced in Section 2.2.

Fig. 4 shows the time evolution of the electron spectrum obtained from the Fokker–Planck model described in Section 2 using the averaged quantities for Family 2 tracer population for Relic B as in Table 3.

Fig. 4 shows the time evolution of the electron energy spectrum for Family 2 population for Relic B. We observe a similar behaviour of the electron energy spectrum evolution as for Relic A. However, since Family 2 population in Relic B is more than one order of magnitude higher than Family 2 population in Relic A, we notice

Table 3. Family-averaged quantities at selected shock times for families in Relic B.

	Time (Gyr)	Mach	B (μG)	ρ (g cm^{-3})	T (K)
Family 1					
Shock 1	13.76	2.7	1.6×10^{-1}	3.1×10^{-28}	6.5×10^{7}
Family 2					
Shock 1	12.82	3.5	1.9×10^{-1}	5.1×10^{-28}	3.2×10^{7}
Shock 2	13.76	2.8	1.4×10^{-1}	2.7×10^{-28}	6.6×10^{7}
Family 3					
Shock 1	12.56	2.4	1.4×10^{-1}	2.8×10^{-28}	1.9×10^{7}
Shock 2	13.31	2.4	3.8×10^{-1}	3.7×10^{-28}	4.0×10^{7}
Shock 3	13.76	2.8	1.5×10^{-1}	2.9×10^{-28}	6.7×10^{7}
Family 4					
Shock 1	7.82	2.3	6.2×10^{-1}	4.9×10^{-28}	1.0×10^{7}
Shock 2	10.98	2.9	2.0×10^{-1}	9.4×10^{-28}	6.4×10^{7}
Shock 3	13.37	2.1	5.6×10^{-1}	6.2×10^{-28}	5.5×10^{7}
Shock 4	13.76	2.3	1.8×10^{-1}	3.4×10^{-28}	7.5×10^{7}

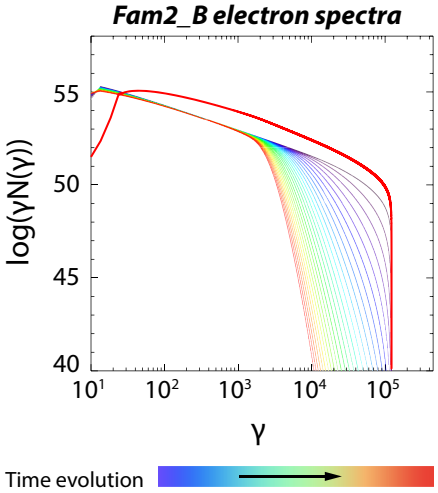

Figure 4. Electron spectra time evolution for quantities-averaged Family 2 tracers for Relic B. Dashed lines correspond to spectra evolution after the first shock. The red solid line represents the electrons spectrum after the second shock.

that the absolute value of the electron energy spectrum for Relic B is approximately one order of magnitude higher than Reilc A spectrum.

Similar electron energy spectrum has been obtained for the other families in Relic B (not shown) in which we observed a behaviour for MS scenario acceleration in the evolution of the spectra consistent with the evolution shown here for Family 2 population.

The family-averaged analysis shown here allowed us to witness the different evolution of MS scenario electron energy spectra compared to a single shock scenario. However, we noticed that the averaged analysis introduced a huge variation in the computation of the electron energy spectra and, subsequently, in the radio emission associated (see Appendix A). In the next section (Section 4), we shall instead compute the detailed radio emission based on the specific sequence of physical fields recorded by each tracer during its evolution, and compute the integrated radio emission across the relic by combining the information of all tracers in all families.

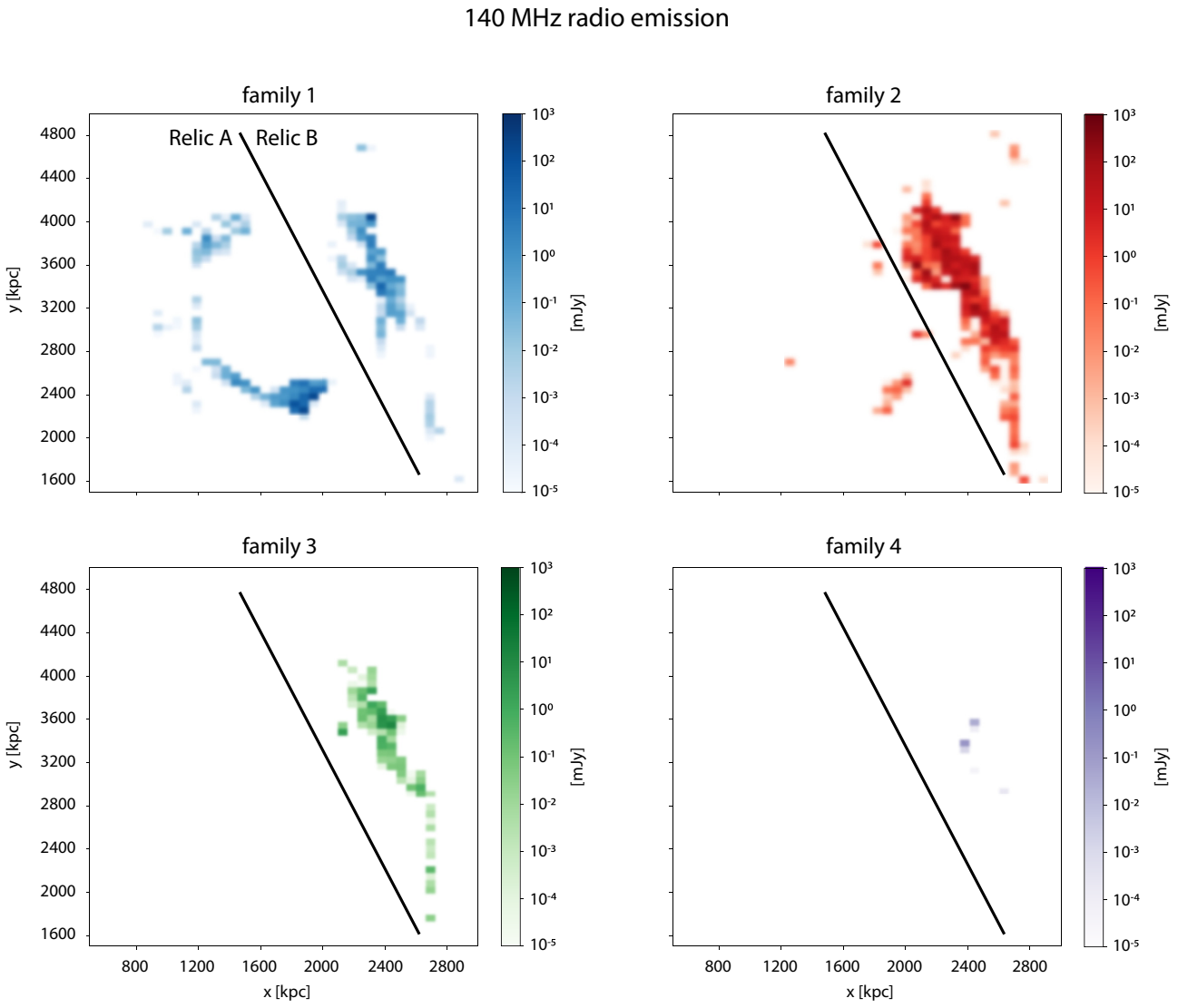

Figure 5. Integrated radio emission (x, y) projection at 140 MHz for Family 1 (top-left), Family 2 (top-right), Family 3 (bottom-left), and Family 4 (bottom-right). The black solid line in the plots divides the particles population between Relic A and Relic B.

4 INTEGRATED RADIO EMISSION

In this section, we study the integrated radio emission along the same viewing angle of Fig. 1, obtained using the electron spectra produced via Fokker–Planck integration over ∼7000 tracers (Section 2). Contrarily to the family-averaged analysis discussed in the previous section, we now compute the energy spectra using the values of density, magnetic field, and density recorded by each tracer. At the final position, we compute the radio emission for both Relic A and Relic B.

Figs 5 and 6 show the integrated radio emission maps, respectively, at 140 MHz and 1.4 GHz, in which we separate the emission contributions from the different families. Assuming the distance of the observation at $z = 0.15$, we calculate the integrated radio emission with a beam size of 63.7 kpc, corresponding to the 25 arcsec LOFAR telescope resolution.

Focusing on Relic A, we see that the integrated radio emission is mostly dominated by Family 1 population and reaches a peak of $\lesssim 10^3$ mJy at 140 MHz, while radio emission of Family 2 is concentrated in the lower-right corner of the relic, and its integrated value is ∼one order of magnitude lower. This makes us conclude that, in Relic A, the visible radio emission will be mostly dominated by Family 1 population, i.e. by newly accelerated electrons. This object appears therefore as a 'classic' powerful radio relic, in which all/most of the observed emission is due to the latest shock, which has energized a pool of fresh electrons, which are being observed within a cooling time since their first acceleration.

Interestingly, the situation is very different for the nearby Relic B, whose integrated radio emission of $\sim 10^3$ mJy at 140 MHz is dominated by the Family 2 population. The electrons from Family 1 and Family 3 are confined in a small sub-volume of Relic B, albeit they have an overall comparable radio emission between each other. The emission for Family 4, instead, due to its smaller occupation fraction, remains negligible at all frequencies.

In Fig. 7, we give the total emission for the 'single' zone analysis of the two relics, i.e. by integrating the CRe emission over the volume of each relic. In a single zone and standard view of radio relics, a $\langle\alpha\rangle \sim -1.55$ associated with a shock with $\mathcal{M} \approx 2.1$. In order for the shock to produce the observed emission of 96 mJy at 1.4 GHz, a single zone Hoeft & Brüggen (2007) method requires to dissipate a fraction in the

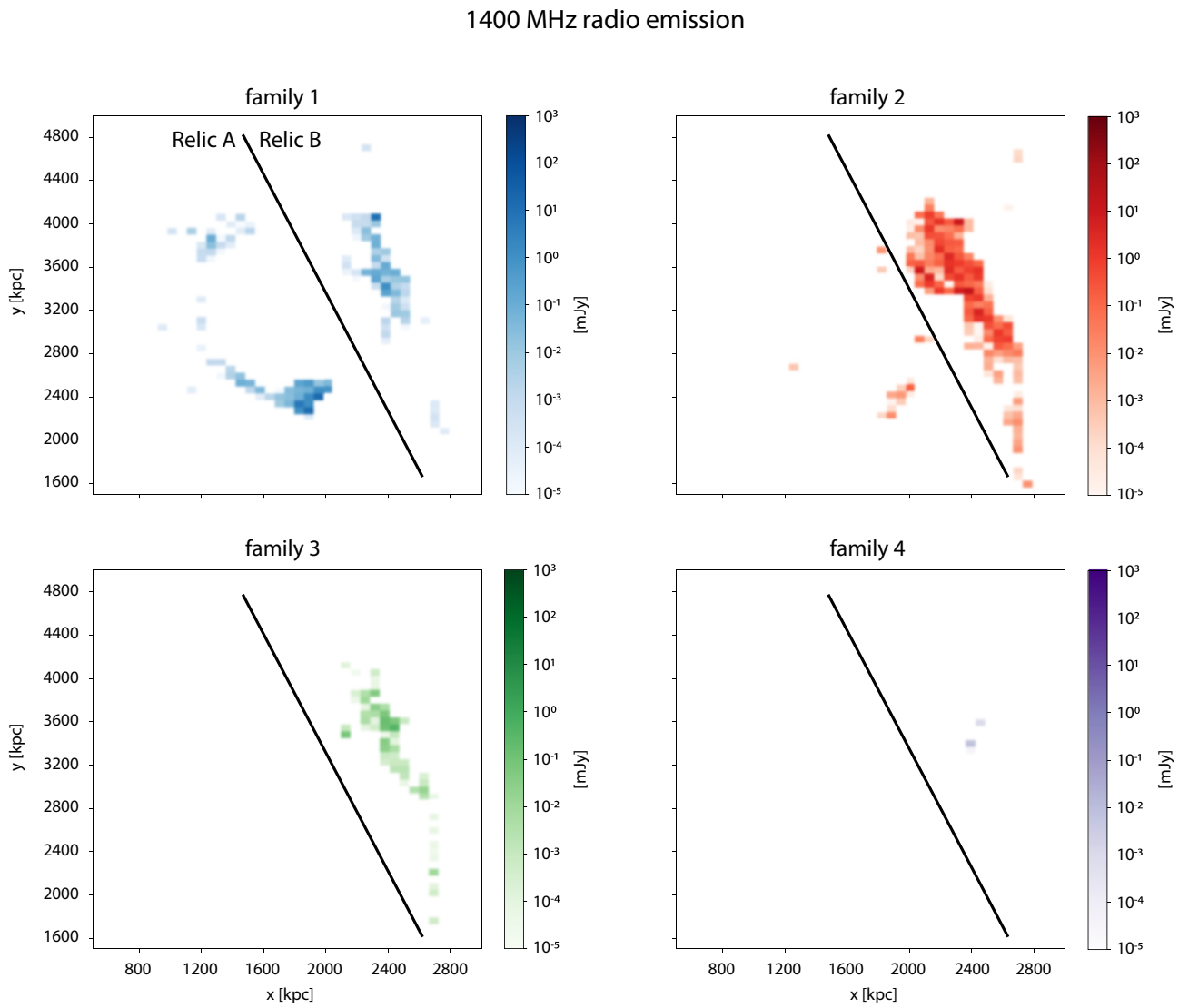

Figure 6. Integrated radio emission (x, y) projection at 1.4 GHz for Family 1 (top-left), Family 2 (top-right), Family 3 (bottom-left), and Family 4 (bottom-right). The black solid line in the plots divides the particles population between Relic A and Relic B.

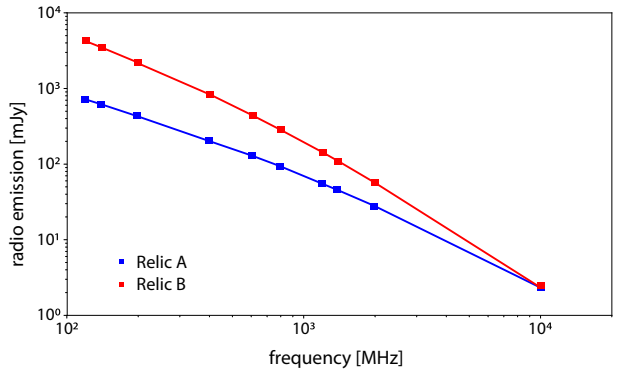

Figure 7. Relic-integrated radio spectrum for Relic A (blue) and Relic B (red).

$K_{\rm inj,e} \approx 3 \times 10^{-4} - 3 \times 10^{-3}$ ballpark of the kinetic energy flux across the shock into electron acceleration – which is very large for such a weak shock, based on DSA (e.g. Kang 2020). This is a common finding of real observations, which have also routinely reported

Table 4. Relics-integrated radio emission.

	Relic A	Relic B
140 MHz	515 mJy	2768 mJy
400 MHz	179 mJy	684 mJy
1.4 GHz	41 mJy	96 mJy

requirements on the acceleration efficiency even of $\sim$ 100 per cent, or larger, in several objects (e.g. Eckert et al. 2016; Stuardi et al. 2019; Botteon et al. 2020). Our analysis instead shows that, even in absence of a nearby active galactic source of radio electrons, sectors of galaxy clusters interested by the MS scenario crossing can boost the emission to a level compatible with observations, due to the re-acceleration of fossil particles injected at a $\leq$0.5–1 Gyr time interval. Detailed values of the single zone radio emission for the two relics at indicative frequencies are reported in Table 4.

We investigate the possibility to observe the simulated relics by comparing the integrated radio emission obtained from the Fokker–Planck model with LOFAR observation properties. Fig. 8 shows the integrated radio emission with the contribution of all the families

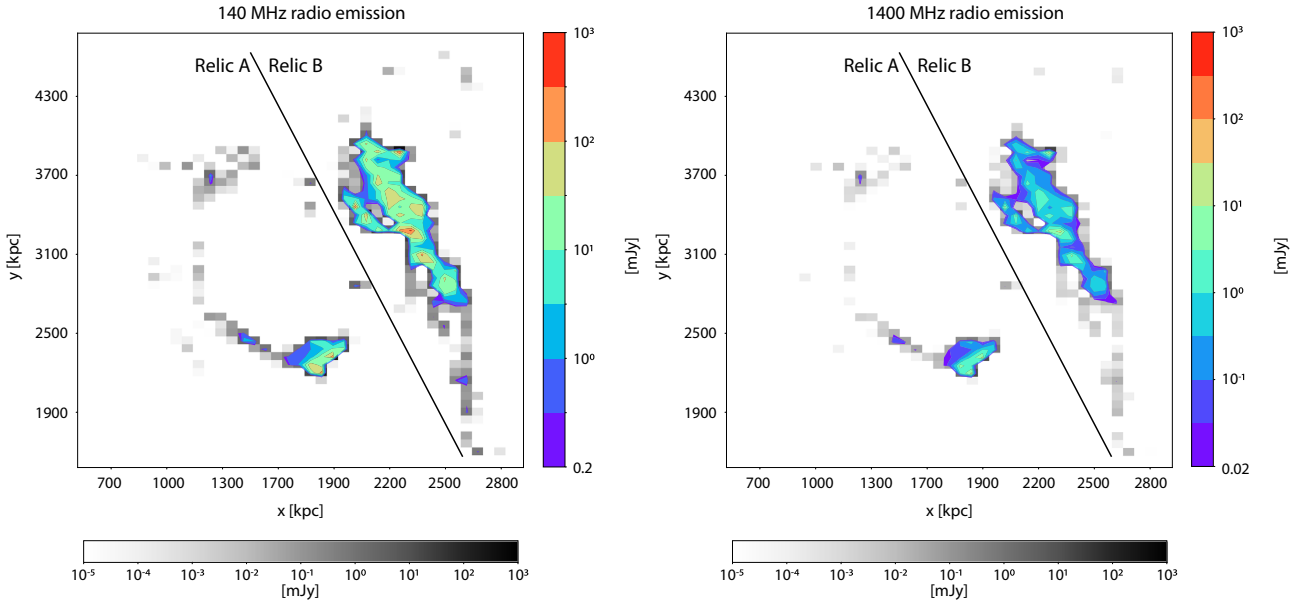

Figure 8. Integrated radio emission for all families at 140 MHz (left) and 1.4 GHz (right) in grey-scale. The coloured contours in the two plots indicate the observable radio flux using the LOFAR threshold of 0.2 mJy at 140 MHz and 0.02 mJy at 1.4 GHz, respectively. The black solid line in the plots divides the particles population between Relic A and Relic B.

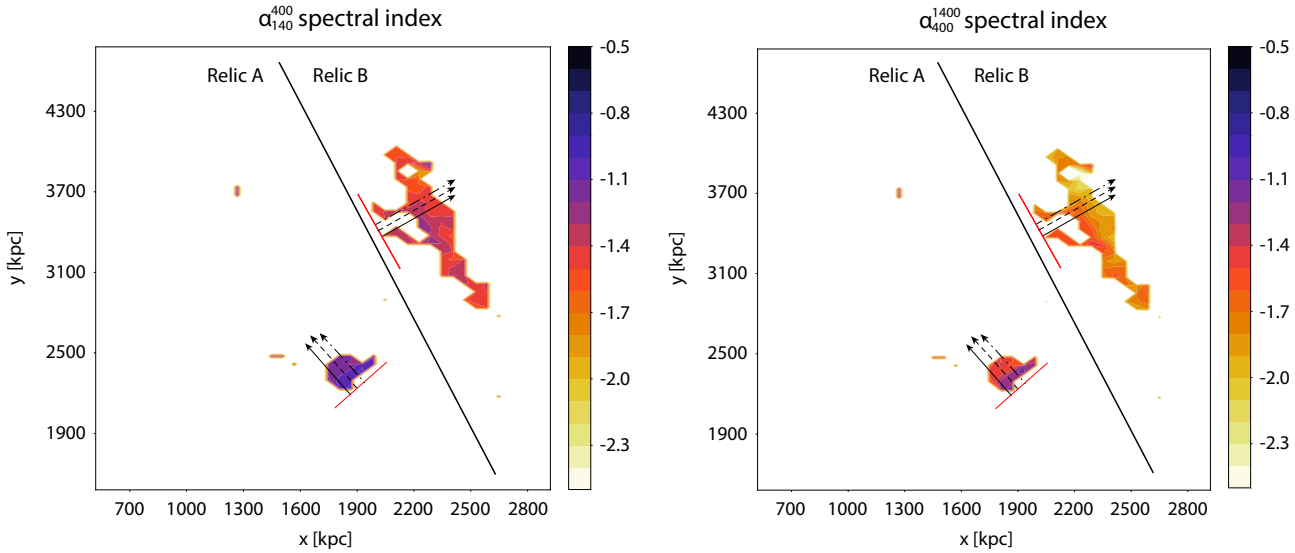

Figure 9. (Left) $\alpha^{400\,\mathrm{MHz}}_{140\,\mathrm{MHz}}$ spectral index map and (right) $\alpha^{1.4\,\mathrm{GHz}}_{400\,\mathrm{MHz}}$ spectral index map from the contribution of all families population. The red lines indicate the position of the shock front for each relic, while the black lines over the relics indicate the lineout of Fig. 10.

in the grey-scale. On top of that, the coloured contours indicate the observable radio emission using the LOFAR threshold of 0.2 mJy at 140 MHz and JVLA threshold of 0.02 mJy at 1.4 GHz, respectively. We can conclude that part of the two radio relics generated in our numerical studies are bright enough to be observable.

4.1 Spectral index map

To investigate possible differences in the spectral index properties at the shock and the energy losses in the post-shock region, we analysed the spectral index profile across the radio relics. We obtain the spectral index map by fitting with a first-order polynomial (i.e. $y = a_1 x + a_0$) the integrated radio emission calculated in Section 4 between frequencies 140 and 400 MHz, and between 400 MHz and 1.4 GHz. For a first-order polynomial fit, the spectral index α is defined as the slope of the fit, i.e. $\alpha = a_1$. Using this first-order fit, we obtain that the radio emission I can be calculated locally at each frequency ν as $I \propto \nu^{\alpha_1}$.

Fig. 9 shows the $\alpha^{400\,\mathrm{MHz}}_{140\,\mathrm{MHz}}$ and $\alpha^{1.4\,\mathrm{GHz}}_{400\,\mathrm{MHz}}$ spectral index maps, obtained from the contribution of all families populations.

The two relics have rather distinct spectral index properties, which may reflect the different histories of shock acceleration in the two cases. Relic A, dominated by Family 1 population, shows a spectral index in the range -1.0 to -1.2 between 140 and 400 MHz and -1.2 to -1.5 between 400 MHz and 1.4 GHz. Relic B, dominated by Family 2 population instead, shows a spectral index in the range of

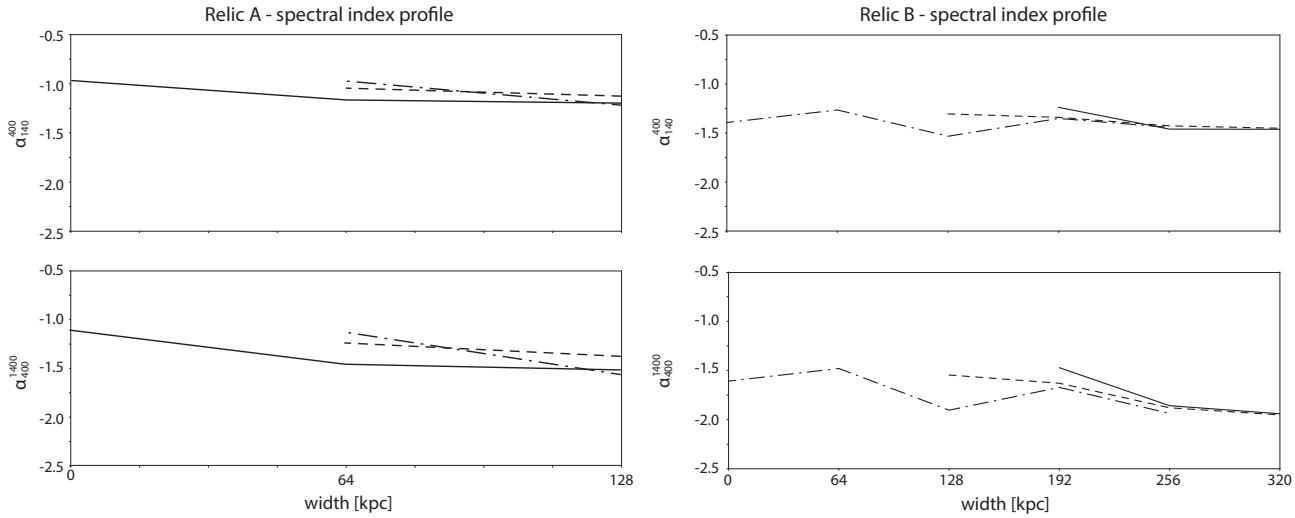

Figure 10. Spectral index profile for Relic A (left) and Relic B (right) between two different frequency ranges. The different black lines correspond to the profile position for each relic as indicated in Fig. 9. The origin of the profiles correspond to the shock front location for each relic.

-1.2 to -1.5 between 140 and 400 MHz and -1.4 to -2.0 between 400 MHz and 1.4 GHz. In particular, the presence of MS acceleration events makes Relic B brighter than Relic A, despite having a steeper radio spectral index.

Fig. 10 shows the spectral index profile for Relic A and Relic B at the line-outs indicated by black lines in Fig. 9. For each relic, we indicated the position of the shock front and its propagation with a red line in Fig. 9 and we compute the line profiles along the direction perpendicular to the shock front, starting at its position. For Relic A, we observe an almost constant distribution of the spectral index along its profile around a value of -1 at low frequency, and at ~-1.2 at high frequency, however the resolution is not high enough for this relic to make a strong statement from such finding. For Relic B, instead, we notice that the spectral index has a generally more fluctuating behaviour, with a steeper radio spectrum at both frequencies, in particular between ~-1.3 and 1.4 at low frequency and between ~-1.5 and 2.0 at high frequency, which remains nearly constant even $\geq$200 kpc away from the shock edge. The latter behaviour appears as a natural consequence of the MS scenario, in the sense that the emission of Relic B is dominated by the low-energy component of re-accelerated electrons, whose radio emission remain high also away from the shock edge. However, since the time elapsed since the epoch of the first injection of electrons in the MS scenario can vary from case to case, depending on the specific accretion history of the host cluster, and on the dynamics in the cluster sector where relics form, different timings of accretions should be reflected in different steepening frequencies for real observed relics.

4.2 Radio colour–colour diagram

The shape of the relativistic electron distribution in radio sources can be studied by means of so-called colour–colour diagrams (Katz-Stone, Rudnick & Anderson 1993; Rudnick & Katz-Stone 1996; Rudnick 2001). These diagrams emphasize the spectral curvature because they represent a comparison between spectral indices calculated at low- and high-frequency ranges. In our case, the low-frequency spectral index values were calculated between 140 and 400 MHz while the high-frequency one between 400 MHz and 1.4 GHz. By this convention, the curvature is negative for a convex spectrum. The resulting colour–colour plots are shown in Fig. 11. The dashed black line indicates a power-law spectrum where $\alpha_{140\,\mathrm{MHz}}^{400\,\mathrm{MHz}} = \alpha_{400\,\mathrm{MHz}}^{1.4\,\mathrm{GHz}}$. Any curve deviating from the power-law line represents a spectrum with changing spectral curvature.

As visible in Fig. 11 (top-left), we find a clear negative curvature as also reported for some of the well-known relics, for example the Toothbrush (Rajpurohit et al. 2020), the Sausage (Di Gennaro et al. 2018), and MACS J0717.5+3745 (Rajpurohit et al. 2021a). The single continuous trajectory in the colour–colour plot suggests that the spectrum also has single shape. We also superimposed the resulting plot with the conventional spectral ageing models, namely JP and KGJP (Komissarov & Gubanov 1994), adopting an injection index of -0.90. The JP model assumes a single burst of particle acceleration and a continued isotropization of the angle between the magnetic field and the electron velocity vectors (the so-called pitch angle) on a time-scale shorter than the radiative time-scale. An extension to the JP model is the KGJP that includes finite time of particle injection.

In Fokker–Planck model (see Section 2) used for the computation of the radio spectra, we use a JP model for the synchrotron energy losses (Jaffe & Perola 1973). At first sight, it may seem surprising that the JP model does never fit the data (Fig. 11). As discussed in Rajpurohit et al. (2020, 2021a), a perfectly edge-on shock front with a uniform magnetic field can be described by the JP model. However, if the shock front is inclined with respect to the line of sight, different spectral ages are present and contribute to the observed spectrum. In this case, the colour–colour distribution follows the KGJP model. As seen in Fig. 11, the KGJP model with an injection index of ≈-0.90 can describe the entire distribution quite well, consistent with what is found for the Toothbrush and the Sausage relics (Di Gennaro et al. 2018; Rajpurohit et al. 2020).

Among the relics, Relic B shows the maximum curvature but both relics follow the same single curve. We do not find any significant difference in the curvature distribution between different families, see Fig. 11. We note that there are no data points in the range -0.5 to -0.90 for both low- and high-frequency spectral index values. This difference can be understood considering that the radio emission properties derived by our Fokker–Planck model have the intrinsic limitation that all particles (even the one injected by the latest shock in the simulation) are evolved at least for one time-step. Hence, even the youngest population of electrons in both our relics has evolved for one

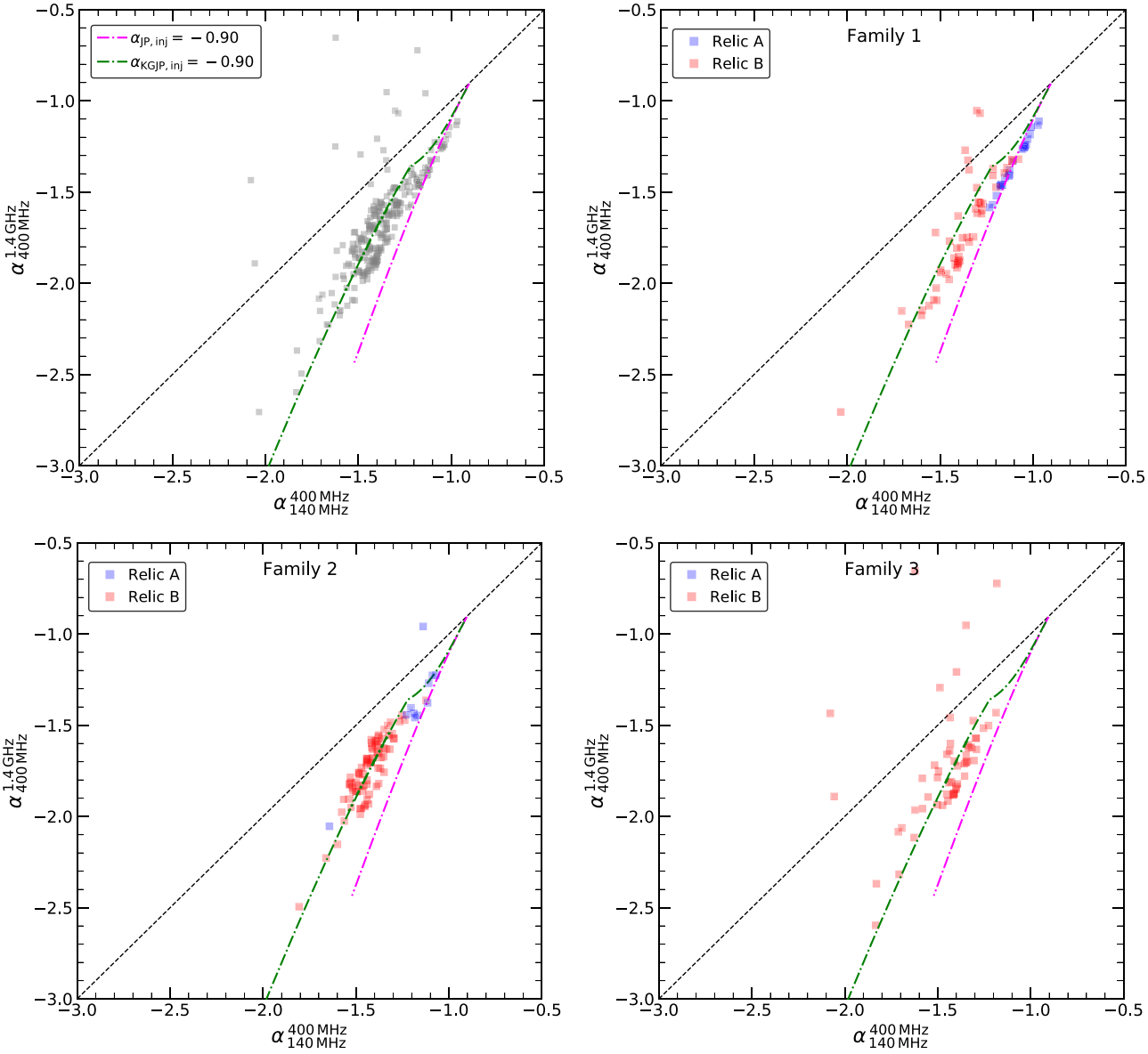

Figure 11. Radio colour–colour plots of the simulated relic superimposed with the spectral ageing JP (magenta) and KGJP (green) models obtained using an injection index of −0.90. For KGJP model, particles are injected continuously for about 16 Myr. Colour–colour plot for all families (top-left), Family 1 (top-right), Family 2 (bottom-left), and Family 3 (bottom-right). The KGJP model fits the distribution well.

time-step after shock injection, with a duration $\Delta t \approx 30$ Myr, and the effects of synchrotron and inverse Compton losses on the observed radio spectrum are already visible at radio emitting frequencies. In summary, the fact that both our relics reasonably well compare with the colour–colour diagrams of real systems (and especially the circumstance that our Relic B is in line with the KGJP model) further confirms that the MS scenario acceleration explored in this work may indeed give rise to realistic relic configurations – albeit non-trivial to tell apart from single injection models, at least based on their colour–colour plots.

5 CONCLUSIONS

We have simulated the evolution of a radio emitting population of relativistic electrons accelerated by multiple merger shock waves, released during the formation of a massive, $M_{200} \approx 9.7 \times 10^{14}\,M_\odot$, galaxy cluster (Wittor et al. 2016, 2017). We focused on the spatial and dynamical evolution of $\sim 10^4$ tracers, which are located in luminous relic-like structures at the end of our run. We assumed DSA as a source of fresh relativistic electrons out of the thermal pool, and applied a Fokker Planck method to integrate their energy evolution under radiative losses, and further re-acceleration events by merger induced shocks. In our scenario, only shock waves can be the source of CRe, yet MS waves sweeping the ICM may produce a pre-acceleration of relativistic electrons, qualitatively similar to what radio galaxies are expected to do (e.g. Markevitch et al. 2005; Kang & Ryu 2011; Macario et al. 2011; Kang et al. 2012, 2014; Pinzke et al. 2013; Botteon et al. 2020). In particular, we indeed identified a specific MS scenario, in which particles cross a shock multiple times, before ending up in realistic ∼Mpc-sized radio relics. Depending on the number of MS events, CRe with a different evolution can become radio visible. This is regardless of the strength of the final shock event. One of our relics (Relic A) is found to be mostly dominated by a population of tracers which were shocked only just before the epoch

of the relic formation, and has a very faint emission, only partially detectable with LOFAR. In this respect, this object appears similar to the recently discovered 'Cornetto' relic (Locatelli et al. 2020), which was suggested to be indeed the prototype of low surface brightness radio relics, only powered by freshly injected electrons.

On the other hand, we measured that the emission by a second relic in the system (Relic B) is dominated by MS scenario accelerated electrons. We use the shock information collected with the tracers to study the evolution of relativistic electrons injected at the shocks and the associated radio emission via the Fokker–Planck solver described in 2.2. We observe that the electron energy spectrum for MS scenario accelerated families differs significantly from the power-law spectrum obtained after a single shock injection, and that their emission is higher than the emission of electrons that were only shocked at the end of the simulation, up to at least ∼1 order of magnitude.

We computed the total radio emission produced by all accelerated electron families in both relics, emulating the threshold parameters of LOFAR telescope at 140 MHz and of the JVLA at 1.4 GHz, obtaining that both relics can be detected by observations, in particular at lower frequencies.

From the analysis of the spectral index maps, we observed that Relic A shows relatively flat spectral index values compared to Relic B, suggesting that the presence of an MS scenario evolution of fossil electrons may influence the slope of the radio spectrum observed in the different relics. The radio colour–colour analysis revealed a single continuous curve for both Relics A and B as well as for all families. The curvature distribution can be well explained by the KGJP model.

This suggests that, at least in systems whose past evolution is characterized by multiple accretion events, for example objects with prominent filamentary accretions and a past with multiple mergers, such as Abell 2744 (Kempner & David 2004; Rajpurohit et al. 2021b), Coma (Brown & Rudnick 2011; Bonafede et al. 2021), and the Toothbrush cluster (van Weeren et al. 2012; Rajpurohit et al. 2020), a significant fraction of the observed radio emission can be the product of MS scenario acceleration, with the effect of an apparent boost of the acceleration efficiency with respect to 'single shock' models. Even if this work is exclusive of a single simulation, we found differences between the radio spectra produced in the MS scenario and the single shock scenario. In particular in the MS scenario, electrons produce a more emission at low frequencies and, hence, a steeper spectrum than the single shock scenario. This is particularly intriguing, as, in the MS scenario, the radio emission is produced without including any other sources of fossil electrons in the ICM. This can soften the assumption that single radio galaxies are the source of fossil electrons, for the observed cases that require a high acceleration efficiency. The MS scenario can indeed produce a large pool of pre-accelerated electrons, with rather similar spectra and energy densities on ∼ Mpc scales, which further produce coherent radio properties on the same scales, if further shocked. The latter may instead be a problem for models in which the source of fossil electrons is a single and recent release of fossil electrons from a radio galaxy. In reality radio galaxies do exist and inject fossil electrons, and we defer the investigation of the MS scenario combined with radio galaxy activity to future work.

ACKNOWLEDGEMENTS

We gratefully acknowledge the very useful feedback by our reviewer, H. Kang, which significantly improved our numerical analysis since our first submitted version. We acknowledge financial support by the European Union's Horizon 2020 program under the ERC Starting Grant 'MAGCOW', no. 714196. DW is funded by the Deutsche Forschungsgemeinschaft (DFG, German Research Foundation) – 441694982. The cosmological simulations were performed with the ENZO code (http://enzo-project.org) and were partially produced at Piz Daint (ETHZ-CSCS, http://www.cscs.ch) in the Chronos project ID ch2 and s585, and on the JURECA supercomputer at the NIC of the Forschungszentrum Jülich, under allocation nos. 7006, 9016, and 9059. For the creation of the NRAO video, GI acknowledge the assistance of $(AM)^2$ research group of Prof. S. Morigi of the Department of Mathematics, University of Bologna and the Visit Lab of A. Guidazzoli of CINECA under the project FIBER OF THE UNIVERSE (http://visitlab.cineca.it/index.php/portfolio/fiber-of-the-universe/). We acknowledge the usage of online storage tools kindly provided by the INAF Astronomical Archive (IA2) initiative (http://www.ia2.inaf.it).

DATA AVAILABILITY

Both the tracer data used for this work[3] and the IDL code used to evolve their energy spectra[4] are publicly available. The ENZO code used to produce the cosmological simulation is also publicly available.[5]

REFERENCES

Ackermann M. et al., 2010, ApJ, 717, L71
Ackermann M. et al., 2014, ApJ, 787, 18
Ackermann M. et al., 2016, ApJ, 819, 149
Akamatsu H., Kawahara H., 2013, PASJ, 65, 16
Akamatsu H. et al., 2017, A&A, 600, A100
Berger M. J., Colella P., 1989, J. Comput. Phys., 82, 64
Blandford R., Eichler D., 1987, Phys. Rep., 154, 1
Bonafede A. et al., 2012, MNRAS, 426, 40
Bonafede A., Giovannini G., Feretti L., Govoni F., Murgia M., 2009, A&A, 494, 429
Bonafede A., Intema H. T., Brüggen M., Girardi M., Nonino M., Kantharia N., van Weeren R. J., Röttgering H. J. A., 2014, ApJ, 785, 1
Bonafede A. et al., 2021, ApJ, 907, 32
Botteon A., Gastaldello F., Brunetti G., Dallacasa D., 2016, MNRAS, 460, L84
Botteon A., Gastaldello F., Brunetti G., 2018, MNRAS, 476, 5591
Botteon A., Brunetti G., Ryu D., Roh S., 2020, A&A, 634, A64
Brown S., Rudnick L., 2011, MNRAS, 412, 2
Brunetti G., Jones T. W., 2014, Int. J. Mod. Phys. D, 23, 1430007
Bryan G. L. et al., 2014, ApJS, 211, 19
Bykov A. M., Vazza F., Kropotina J. A., Levenfish K. P., Paerels F. B. S., 2019, Space Sci. Rev., 215, 14
Canning R. E. A. et al., 2017, MNRAS, 464, 2896
Chang J. S., Cooper G., 1970, J. Comput. Phys., 6, 1
Colella P., Glaz H. M., 1985, J. Comput. Phys., 59, 264
Dedner A., Kemm F., Kröner D., Munz C.-D., Schnitzer T., Wesenberg M., 2002, J. Comput. Phys., 175, 645
Di Gennaro G. et al., 2018, ApJ, 865, 24
Di Gennaro G. et al., 2019, ApJ, 873, 64
Eckert D., Jauzac M., Vazza F., Owers M. S., Kneib J. P., Tchernin C., Intema H., Knowles K., 2016, MNRAS, 461, 1302
Ensslin T. A., Biermann P. L., Klein U., Kohle S., 1998, A&A, 332, 395
Fermi E., 1949, Phys. Rev., 75, 1169
Gabici S., Blasi P., 2003, ApJ, 583, 695

[3] https://owncloud.ia2.inaf.it/index.php/s/zcskRy1bryHN62i
[4] https://github.com/FrancoVazza/IDL_FP
[5] enzo-project.org

Genel S., Vogelsberger M., Nelson D., Sijacki D., Springel V., Hernquist L., 2013, MNRAS, 435, 1426
Giacintucci S. et al., 2008, A&A, 486, 347
Guo X., Sironi L., Narayan R., 2014, ApJ, 797, 47
Ha J.-H., Ryu D., Kang H., van Marle A. J., 2018, ApJ, 864, 105
Ha J.-H., Ryu D., Kang H., 2020, ApJ, 892, 86
Ha J.-H., Kim S., Ryu D., Kang H., 2021, ApJ, 915, 18
Hoang D. N. et al., 2017, MNRAS, 471, 1107
Hockney R. W., Eastwood J. W., 1988, Computer Simulation Using Particles. Hilger, Bristol
Hoeft M., Brüggen M., 2007, MNRAS, 375, 77
Hong S. E., Kang H., Ryu D., 2015, ApJ, 812, 49
Jaffe W. J., Perola G. C., 1973, A&A, 26, 423
Kang H., 2020, J. Korean Astron. Soc., 53, 59
Kang H., 2021, J. Korean Astron. Soc., 54, 103
Kang H., Ryu D., 2011, ApJ, 734, 18
Kang H., Ryu D., Jones T. W., 2012, ApJ, 756, 97
Kang H., Petrosian V., Ryu D., Jones T. W., 2014, ApJ, 788, 142
Kang H., Ryu D., Ha J.-H., 2019, ApJ, 876, 79
Kardashev N. S., 1962, Sov. Astron., 6, 317
Katz-Stone D. M., Rudnick L., Anderson M. C., 1993, ApJ, 407, 549
Kempner J. C., David L. P., 2004, MNRAS, 349, 385
Komissarov S. S., Gubanov A. G., 1994, A&A, 285, 27
Locatelli N. T. et al., 2020, MNRAS, 496, L48
Macario G., Markevitch M., Giacintucci S., Brunetti G., Venturi T., Murray S. S., 2011, ApJ, 728, 82
Markevitch M., Govoni F., Brunetti G., Jerius D., 2005, ApJ, 627, 733
Park J., Caprioli D., Spitkovsky A., 2015, Phys. Rev. Lett., 114, 085003
Pinzke A., Oh S. P., Pfrommer C., 2013, MNRAS, 435, 1061
Rajpurohit K. et al., 2018, ApJ, 852, 65
Rajpurohit K. et al., 2020, A&A, 636, A30
Rajpurohit K. et al., 2021a, A&A, 646, A56
Rajpurohit K. et al., 2021b, A&A, 654, A41
Roettiger K., Stone J. M., Burns J. O., 1999, ApJ, 518, 594
Rudnick L., 2001, in Laing R. A., Blundell K. M., eds, ASP Conf. Ser. Vol. 250, Particles and Fields in Radio Galaxies Conference. Astron. Soc. Pac., San Francisco, p. 372
Rudnick L., Katz-Stone D., 1996, Powerful Diagnostics of Cygnus A's Relativistic Electrons, Cambridge University Press, Cambridge
Ryu D., Kang H., Ha J.-H., 2019, ApJ, 883, 60
Sarazin C. L., 1999, ApJ, 520, 529
Shimwell T. W., Markevitch M., Brown S., Feretti L., Gaensler B. M., Johnston-Hollitt M., Lage C., Srinivasan R., 2015, MNRAS, 449, 1486
Stuardi C. et al., 2019, MNRAS, 489, 3905
Uchiyama Y., Aharonian F. A., Tanaka T., Takahashi T., Maeda Y., 2007, Nature, 449, 576
van Weeren R. J., Röttgering H. J. A., Brüggen M., Hoeft M., 2010, Science, 330, 347
van Weeren R. J., Röttgering H. J. A., Intema H. T., Rudnick L., Brüggen M., Hoeft M., Oonk J. B. R., 2012, A&A, 546, A124
van Weeren R. J. et al., 2016, ApJ, 818, 204
van Weeren R. J. et al., 2017, Nat. Astron., 1, 0005
van Weeren R. J., de Gasperin F., Akamatsu H., Brüggen M., Feretti L., Kang H., Stroe A., Zandanel F., 2019, Space Sci. Rev., 215, 16
Vazza F., Brüggen M., 2014, MNRAS, 437, 2291
Vazza F., Eckert D., Brüggen M., Huber B., 2015, MNRAS, 451, 2198
Vazza F., Brüggen M., Wittor D., Gheller C., Eckert D., Stubbe M., 2016, MNRAS, 459, 70
Vazza F., Brunetti G., Brüggen M., Bonafede A., 2018, MNRAS, 474, 1672
Vazza F., Wittor D., Brunetti G., Brüggen M., 2021, A&A, 653, A23
Wittor D., 2017, PhD thesis, Universität Hamburg, Von-Melle-Park, Hamburg, http://ediss.sub.uni-hamburg.de/volltexte/2018/8914
Wittor D., 2021, New Astron., 85, 101550
Wittor D., Vazza F., Brüggen M., 2016, Galaxies, 4, 71
Wittor D., Vazza F., Brüggen M., 2017, MNRAS, 464, 4448
Wittor D., Vazza F., Ryu D., Kang H., 2020, MNRAS, 495, L112
Wittor D., Ettori S., Vazza F., Rajpurohit K., Hoeft M., Domínguez-Fernández P., 2021, MNRAS, 506, 396
Xu R., Spitkovsky A., Caprioli D., 2020, ApJ, 897, L41
Zhang C., Churazov E., Dolag K., Forman W. R., Zhuravleva I., 2020, MNRAS, 498, L130
Zhang C., Churazov E., Zhuravleva I., 2021, MNRAS, 501, 1038

APPENDIX A: AVERAGED MS SCENARIO RADIO EMISSION

In this section, we describe in more details the radio emission obtained from the family-averaged analysis introduced in Section 3.

A1 Relic A

Fig. A1 shows the time evolution of the number of shocked tracers, the averaged Mach number, the averaged magnetic field, the averaged temperature, and the averaged density for both Family 1 (blue) and Family 2 (red) for Relic A. The vertical dashed lines mark the shock times chosen to represent each family.

Using the electron energy spectrum obtained at $t_{\rm end}$, we compute the radio spectrum associated for each family. We numerically integrated the synchrotron emission from tracers assuming the Jaffe Perola (JP) ageing model (Jaffe & Perola 1973), and we placed our cluster at the approximate distance of the Coma cluster (i.e. ≈ 100 Mpc). In particular, we weight the spectra according to the relative population of the corresponding family. Fig. A2 shows the electron energy spectra (left) and radio spectra (right) at $t_{\rm end}$ for the family-averaged quantities for Family 1 (blue) and Family 2 (red) in Relic A. The wide red area in the plot shows the range of variability of the Family 2 spectra using the $\pm\sigma$ values of the averaged quantities as input parameters, where σ is the standard deviation. The standard deviation parameters are reported in Table A1

To consider the radio emission variance associated with the family-averaged analysis, we present as case of study the variability for Family 2. As we are going to present in this section, the results obtained from this analysis induced to proceed with the more detailed tracer integration analysis introduced in Section 4. For this reason, we did not proceed to compute the averaged quantities for the other families.

We observe that the radio spectra obtained from the family-averaged analysis at $t_{\rm end}$ have similar slope for the two families. However, the variation of the radio spectrum obtained using the standard deviation makes difficult to clarify if Family 2 has an higher emission than Family 1.

A2 Relic B

Fig. A3 shows the time evolution of the number of shocked tracers, the averaged Mach number, the averaged magnetic field, the averaged temperature, and the averaged density for Family 1 (blue), Family 2 (red), Family 3 (green), and Family 4 (orange) for Relic B. The vertical dashed lines mark the shock epochs chosen to represent each family in the population-averaged analysis.

Using the electron energy spectrum obtained at $t_{\rm end}$, we compute the radio spectrum associated with each family. Fig. A4 shows the electron energy spectra (left) and radio spectra (right) at $t_{\rm end}$ for the averaged quantities for Family 1 (blue), Family 2 (red), Family 3 (green), and Family 4 (orange) in Relic B. The wide red area in the plot shows the range of variability of Family 2 spectra using, as input parameters, the $\pm\sigma$ values of the averaged quantities. The standard deviation parameters are reported in Table A2

We notice that the electron energy spectra for MS scenario families at the final stage of the simulation have a knee around $\gamma \sim 10^3$. Since

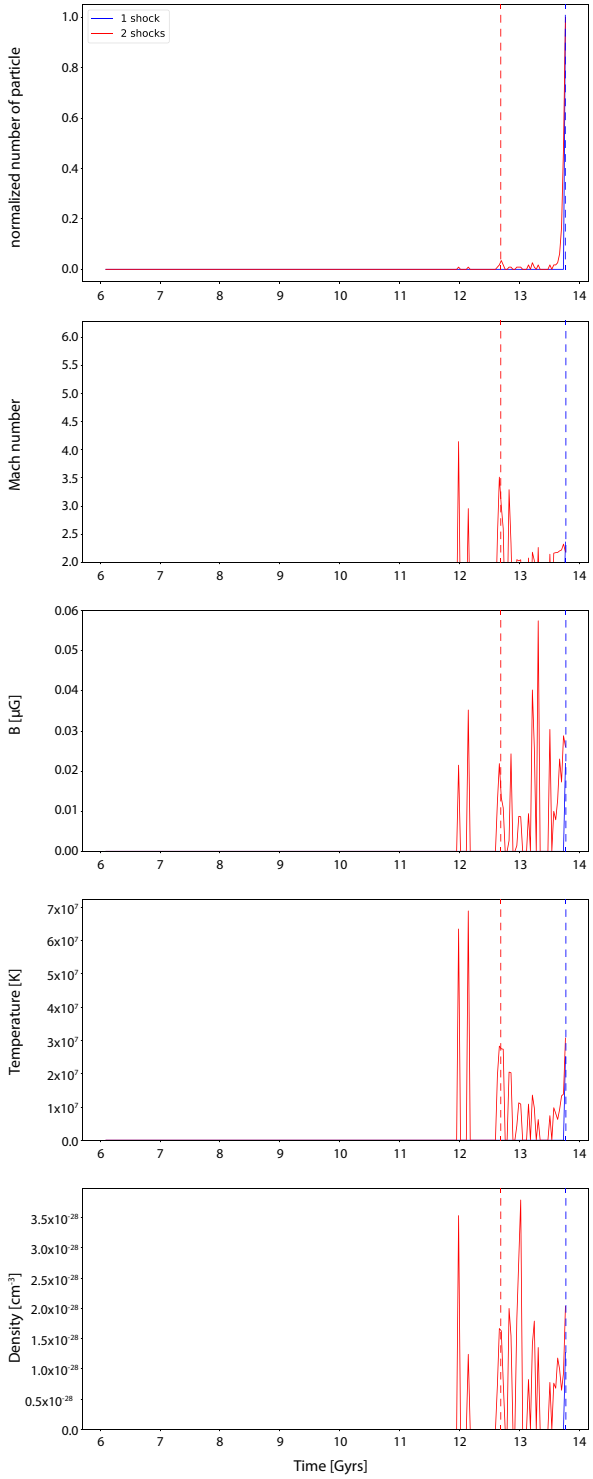

Figure A1. From top to bottom: Time evolution of the number of shocked tracers, the averaged Mach number, the averaged magnetic field, the averaged temperature, and the averaged density for both Family 1 (blue) and Family 2 (red) for Relic A. The vertical dashed lines mark the shock times chosen to represent each family.

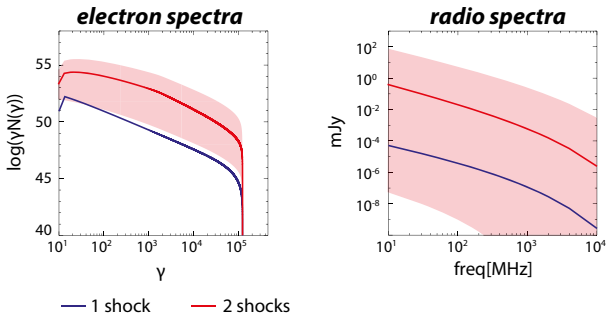

Figure A2. Electron energy spectra (left) and radio spectra (right) at t_{end} for the population-averaged quantities for Family 1 (blue) and Family 2 (red) in Relic A. The wide red area shows the range of variability of Family 2 spectra using the $\pm\sigma$ values of the averaged quantities as input parameters.

Table A1. Standard deviation σ associated with Family 2-averaged quantities in Relic A.

	Time (Gyr)	Mach	B (μG)	ρ (g cm^{-3})	T (K)
Family 2					
Shock 1	12.69	±1.2	±1.2e−02	±5.2e−29	±2.7e+07
Shock 2	13.76	±0.4	±2.1e−01	±1.2e−28	±1.0e+07

the radio emission is more relevant for high energies of the electron spectrum, the slope of the radio spectra is similar for all families, but Family 2 radio emission dominates over the others by a few orders of magnitude, reaching a peak of ∼0.1 mJy at ∼100 MHz. However, as for Relic A, the variation of the radio spectrum obtained using the standard deviation makes difficult to clarify if Family 2 has an higher emission than the other families.

The results obtained from the family-averaged analysis of the two relics induced to proceed with the more detailed tracer integration analysis introduced in Section 4. For this reason, we did not proceed to compute the averaged quantities for the other families.

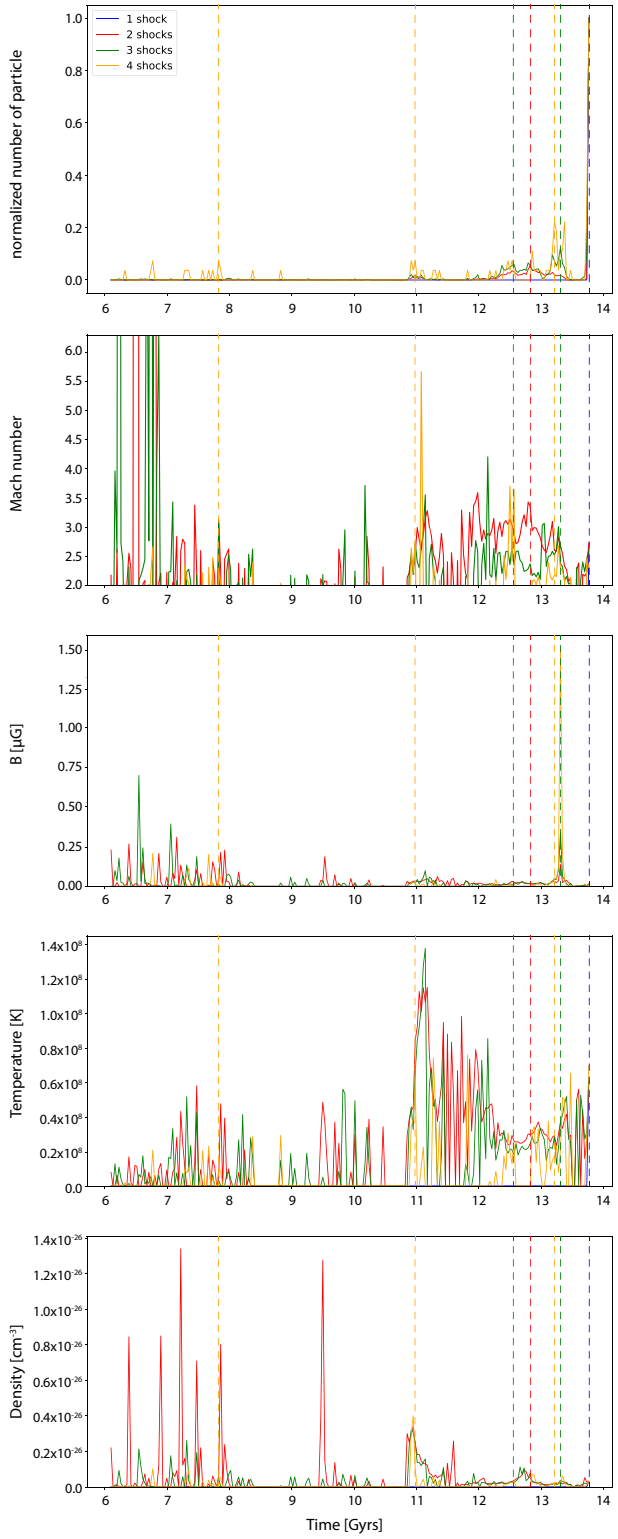

Figure A3. From top to bottom: Time evolution of the number of shocked tracers, the averaged Mach number, the averaged magnetic field, the averaged temperature, and the averaged density for Family 1 (blue), Family 2 (red), Family 3 (green), and Family 4 (orange) for Relic B. The vertical dashed lines mark the shock times chosen to represent each family.

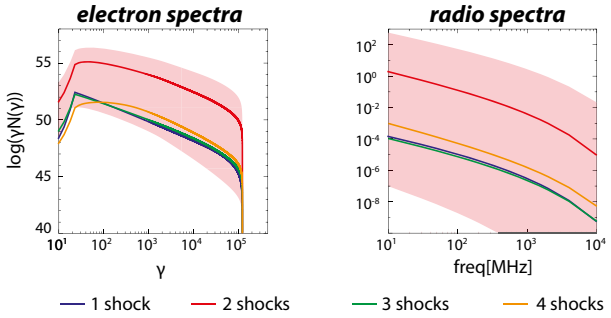

Figure A4. Electron energy spectra (left) and radio spectra (right) at t_{end} for the averaged quantities for Family 1 (blue), Family 2 (red), Family 3 (green), and Family 4 (orange) in Relic B. The wide red area shows the range of variability of Family 2 spectra using the $\pm\sigma$ values of the averaged quantities as input parameters.

Table A2. Standard deviation σ associated with Family 2-averaged quantities in Relic B.

	Time (Gyr)	Mach	B (μG)	ρ (g cm^{-3})	T (K)
Family 2					
Shock 1	12.69	±1.0	±9.4e−02	±5.0e−28	±8.4e+06
Shock 2	13.76	±0.9	±1.1e−01	±1.5e−28	±2.3e+07

This paper has been typeset from a TEX/LATEX file prepared by the author.